minerals

MDPI

Article

Ore Genesis of the Langcun Porphyry W-Mo Deposit, South China: Constraints from Fluid Inclusion and H-O-S Isotopics

Kai Cui [1,2], Yunwei Qu [3,*], Yuling Xie [3], Kejun Yang [4] and Zhaoqiang Huang [1]

[1] Institute of Mineral Recourses Research, China Metallurgical Geology Bureau, Beijing 101300, China; cuikai@cmgb.cn (K.C.); huangzhaoqiang@cmgb.cn (Z.H.)
[2] School of Earth Sciences and Resources, China University of Geosciences (Beijing), Beijing 100083, China
[3] Civil and Resource Engineering School, University of Science and Technology Beijing, Beijing 100083, China; yulingxie63@hotmail.com
[4] Jiangxi Copper (Hong Kong) Investment Co., Ltd., Beijing 100020, China; kejun.y@outlook.com
* Correspondence: yunwei.qu@outlook.com

Abstract: The Langcun W-Mo deposit, located in the Zhejiang Province of South China, is a medium-sized porphyry deposit. The ore bodies mainly occur in aplite, granite porphyry, and the contact zone with hornfels of the Nanhua System. Four stages of mineralization are recognized in the Langcun deposit, including the quartz–K-feldspar stage (stage I), quartz–sericite–molybdenite stage (stage II), quartz–chlorite–pyrite stage (stage III), and calcite stage (stage IV). Stages I and II are the main ore-forming stages for wolframite and molybdenite. The petrographic and microthermometric results show that four types of fluid inclusions exist in the Langcun W-Mo deposit, including two-phase liquid-rich fluid inclusions (type LV), three-phase CO_2-rich fluid inclusions (type LC), pure CO_2 fluid inclusions (type C), vapor H_2O inclusions (type V), and multi-phase inclusions with daughter minerals (type LDV). In stage I, the fluid inclusion assemblage is LDV + LV + V, and the LDV and LV fluid inclusions have similar homogenization temperatures (281–387 °C), indicating a boiling fluid inclusions association. In stage II, the fluid inclusion assemblage is LC + C, indicating immiscibility between CO_2 and aqueous fluids. The homogenization temperatures of type LC are in the range of 228–342 °C, and the salinities are in the range of 2.77–5.14 wt.% NaCl equiv. The fluid inclusions in stages III and IV are type LV, with homogenization temperatures in the ranges of 224–275 °C and 200–225 °C, respectively, and salinities in the ranges of 1.74 to 4.96 wt.% NaCl equiv and 1.06 to 3.39 wt.% NaCl equiv, respectively. Hydrogen and oxygen isotopic results indicate that the ore-forming fluids mainly come from magmatic water in the early stage and may have received an input of meteoric water in the late stage, which results in the decrease in the temperature and salinity of ore-forming fluid. Early W-Mo precipitation was induced by CO_2 escape because of decompression, and fluid mixing resulted in Mo precipitation in the later stage.

Keywords: Langcun W-Mo deposit; fluid inclusion; H-O-S isotope; W-Mo precipitation

check for updates

Academic Editor: Pierfranco Lattanzi

Received: 20 November 2024
Revised: 21 January 2025
Accepted: 21 January 2025
Published: 23 January 2025

Citation: Cui, K.; Qu, Y.; Xie, Y.; Yang, K.; Huang, Z. Ore Genesis of the Langcun Porphyry W-Mo Deposit, South China: Constraints from Fluid Inclusion and H-O-S Isotopics. *Minerals* **2025**, *15*, 109. https://doi.org/10.3390/min15020109

1. Introduction

The South China W-Sn metallogenic province is renowned for its substantial resources of tungsten (W) and tin (Sn), contributing more than 60% and 11% of the global reserves, respectively [1,2]. The majority of the W polymetallic deposits are intimately associated with Mesozoic granitoids [3,4]. The predominant deposit types in South China are skarn (e.g., the Shizhuyuan W-polymetallic deposit [5]), greisen and quartz-vein (e.g., the Hongshuizhai deposit [6]), and porphyry (e.g., the

Yangchuling deposit [7]). Skarn and greisen–quartz-vein deposits have historically accounted for over 90% of identified tungsten resources. In recent years, the discovery of several giant porphyry W deposits, such as Dahutang [8], Dongyuan [9], and Xingluokeng [10], has highlighted the significance of porphyry systems. Despite these advancements, there is currently limited research on fluid inclusions in porphyry W deposits. Fluid inclusion studies are fundamental to understand the nature and evolutionary process of the ore-forming fluids in porphyry W deposits, and for the overall understanding of their genesis. In turn, this knowledge has important consequences for the research.

Langcun is a medium-size porphyry tungsten–molybdenum (W-Mo) deposit that was recently identified in South China, and it hosts significant resources with 18,500 tonnes of WO_3. The mineralization of tungsten and molybdenum is predominantly as veins and stockworks within the aplite, granite porphyry, and surrounding rocks. Aplite is characterized by the presence of quartz–K-felspar druses, within which molybdenite occurs. Based on our detailed field observation, we conducted petrological, mineralogical, fluid inclusions, and stable isotopic analysis for the ore host granite porphyry, aplite, hydrothermal veins, and altered rocks. The findings reveal that the ore-forming fluids are CO_2-rich NaCl-H_2O fluids, marked by a relatively high temperature (~387 °C), high to medium salinities, and are predominantly derived from magmatic water. These research results have a direct and profound impact on guiding mineral exploration and improving exploration efficiency.

2. Geological Setting

2.1. Regional Geology

The Langcun W-Mo deposit is located in the southeastern part of the Yangtze Block, which is part of the South China Block (Figure 1). Tectonically, the South China Block was formed by the amalgamation of the Yangtze Block and Cathaysia Block during the Neoproterozoic era (ca. 850 Ma) (Figure 1) [11–13]. The region has undergone multi-phase tectonic–magmatic events. Notably, the most significant was associated with the Mesozoic subduction of the Paleo-Pacific plate beneath the South China Block, which resulted in a shift in the tectonic regime from the Tethys to the Paleo-Pacific [14–16]. Subsequently, alterations in the subduction angle of the Pacific plate shifted the tectonic setting from compression to extension, prompting lithospheric thinning and consequent extensive granitic magmatism and mineralization [17,18]. The transition is estimated to have begun around ca. 145 Ma [19] and lasted to approximately ca. 123 Ma. During this period, the South China Block entered a post-collisional phase, as evidenced by the emergence of extensive A-type granites and the diabase dike along the southern margin of the Yangtze Block [20–23].

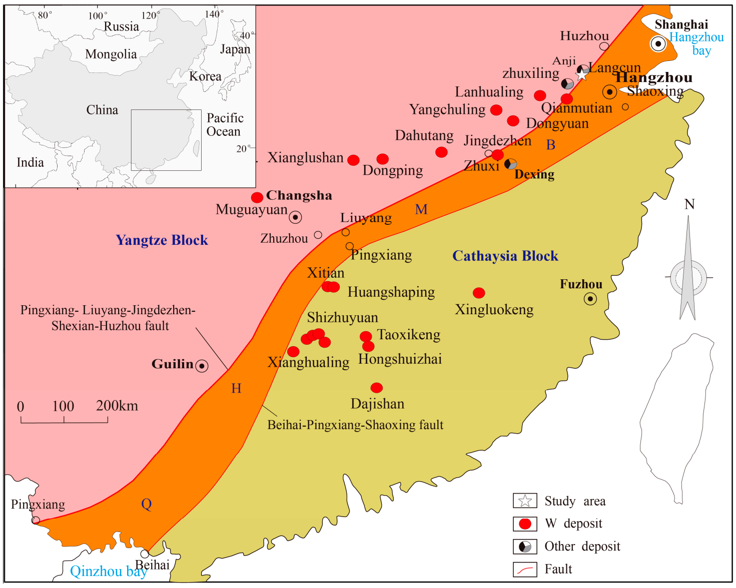

Figure 1. Distribution of the major W deposits in South China (modified from [24]).

2.2. Ore Deposit Geology

The Langcun W-Mo deposit, located in Anji County in Zhejiang Province in northwest South China, is characterized by diverse lithological units. The dominant units in the region include the Nanhua, Sinian, Cambrian, Silurian, Cretaceous, and Quaternary Systems (Figure 2) [25]. The Xiuning Formation, which is mainly silty hornfels and greywacke, is overlain by the manganese dolomite-bearing sandstone of the Nantuo Formation. The Doushantuo Formation is composed of siliceous rock and hornfels. The Dengying Formation with marbleized dolomite overlies the Doushantuo Formation. The Hetang Formation consists of interbedded shale and siliceous rock, while the Dachenling Formation comprises lime dolostone and thin layers of siliceous rock. The Yangliugang Formation is predominantly limestone. The Xiaxiang Formation consists of interbeds of siltstone and silty mudstone, which are an unconformity in relation to the clastic sedimentary and volcaniclastic rocks of the Laocun Formation. The area is crisscrossed by multiple fault systems, including NE-trending major thrusts, such as F1 and F3, and the NW-trending F2 fault (Figure 2). Furthermore, a series of secondary NE and NW trending faults have developed in the region, significantly influencing the occurrence and distribution of wolframite and molybdenite–quartz veins.

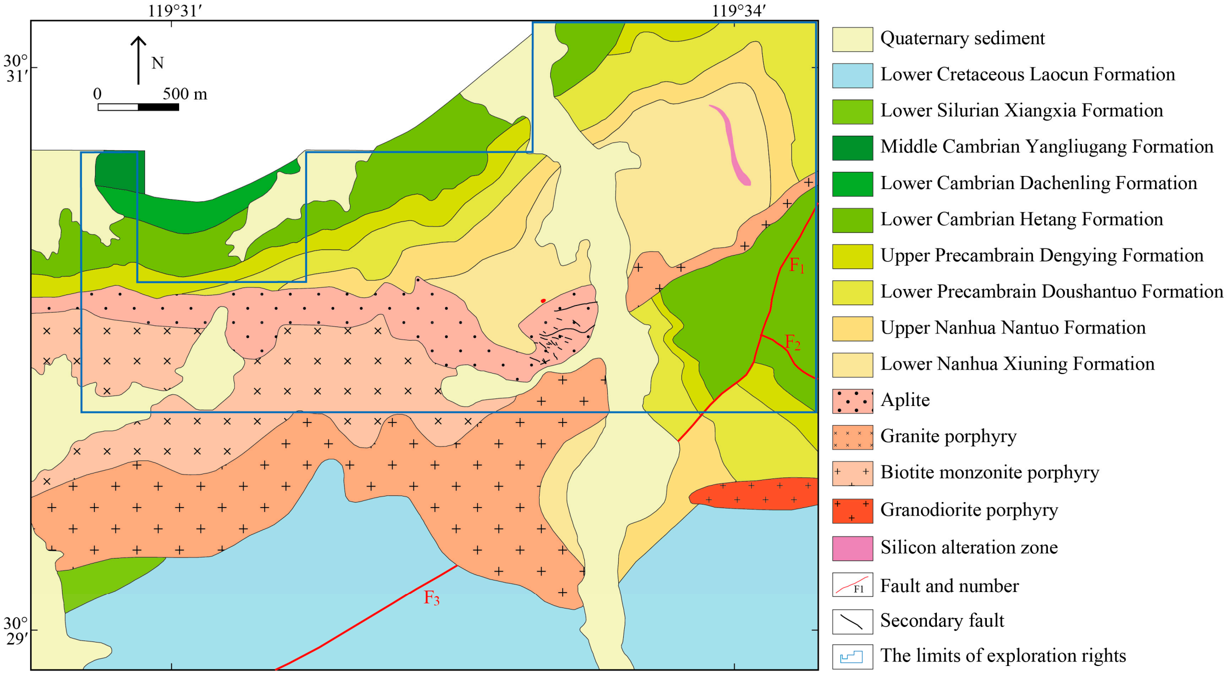

Figure 2. Simplified geologic map of the Langcun deposit (modified from [25]).

The Yanshanian magmatism was intense in the Langcun area, and is characterized by the presence of various intrusions, such as biotite monzonite porphyry, aplite, granite porphyry, and lamprophyre dykes. Aplite often occurs together with lamprophyre (Figure 3a), which can be observed cutting through biotite monzonite porphyry. These intrusions are often associated with quartz–K-feldspar–epidote druses and veins, indicating hydrothermal activity (Figure 3b,c). The zircon LA-ICP-MS U-Pb ages of these intrusions have yielded age values predominantly ranging from 144 to 132 Ma [26]. These data correlate well with the LA-ICP-MS U-Pb age of 127 Ma obtained from wolframite [26], suggesting a late-Mesozoic W mineralization event in the region.

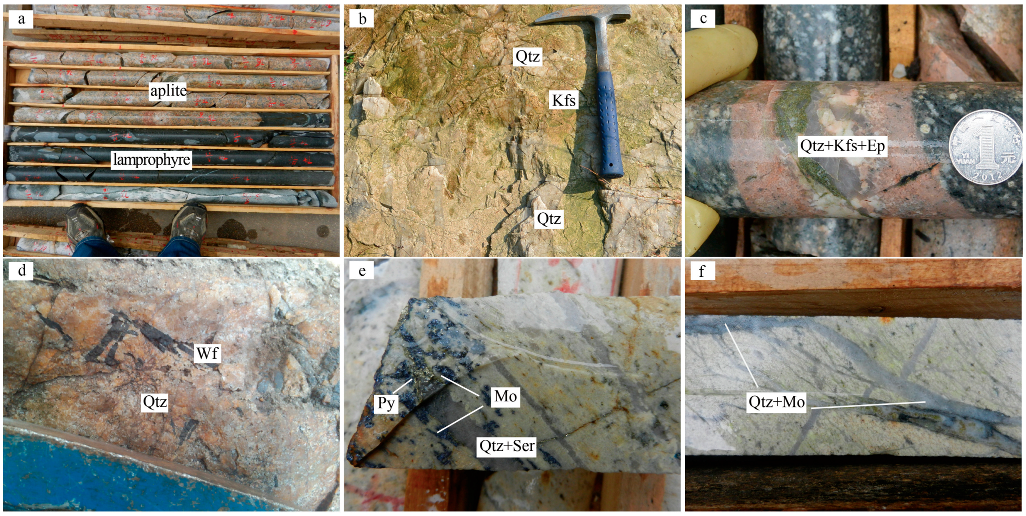

Figure 3. Photographs showing the ore geology and mineralization of the Langcun W-Mo deposit. (**a**) Aplite occurs together with lamprophyre; (**b**) quartz–K-feldspar druses occur in aplite; (**c**) quartz–K-feldspar–epidote veins occur in aplite; (**d**) wolframite occurs as disseminations in aplite; (**e**) molybdenite occurs as disseminations and veins in aplite; (**f**) quartz–molybdenite stockworks in aplite. Abbreviations: Ep—epidote; Kfs—K-feldspar; Mo—molybdenite; Py—pyrite; Qtz—quartz; Ser—sericite; Wf—wolframite.

2.3. Mineralization

The mineralization of wolframite and molybdenite mainly occurs within aplite and granite porphyry, with minor occurrences in hornfels (Figure 3d–f). Twenty wolframite vein ore bodies have been identified in the mine, with an average grade of 1.25% WO_3 and an estimated resource of 18,500 t of WO_3. Additionally, minor scheelite ore bodies in the Xiuning Formation have been observed, with an average grade of 0.153% WO_3. Molybdenite's mineralization, often associated with wolframite, is yet to be fully assessed for its resource potential. Mineralization appears as disseminated (Figure 3d,e), stockworks (Figure 3f), and veins (Figure 3e). Disseminated wolframite and molybdenite primarily occur in aplite and granite porphyry, while vein and stockwork types are the main types of W and Mo mineralization in the region, such as wolframite veins, quartz–wolframite veins, molybdenite veins, quartz–molybdenite ± pyrite veins, and quartz–sulfide–wolframite veins. These veins are composed of quartz, fluorite, wolframite, molybdenite, pyrite, magnetite, and minor amounts of chalcopyrite, pyrrhotite, galena, and sphalerite.

The host rock experienced extensive hydrothermal alterations in the Langcun deposit, including K-feldsparization, silicification, sericitization, chloritization, epidotization, and carbonation, among which silicification and sericitization are particularly associated with W and Mo mineralization. A field observation of vein crosscutting relationships, alteration patterns, and the mineral assemblages in the deposit suggests four continuous mineralization stages:

Stage I: Quartz–K-feldspar stage.

The main tungsten mineralization stage is characterized by quartz–K-feldspar veins and druses occurring within the aplite (Figure 3b,c and Figure 4a). The mineral assemblage includes quartz, K-feldspar, wolframite, and scheelite, and a small amount of molybdenite (Figure 5a,b).

Stage II: Quartz–sericite–molybdenite stage.

This stage includes the main molybdenite mineralization, in which the mineral assemblages are dominated by quartz, sericite, molybdenite, pyrite, and pyrrhotite (Figure 5c,d).

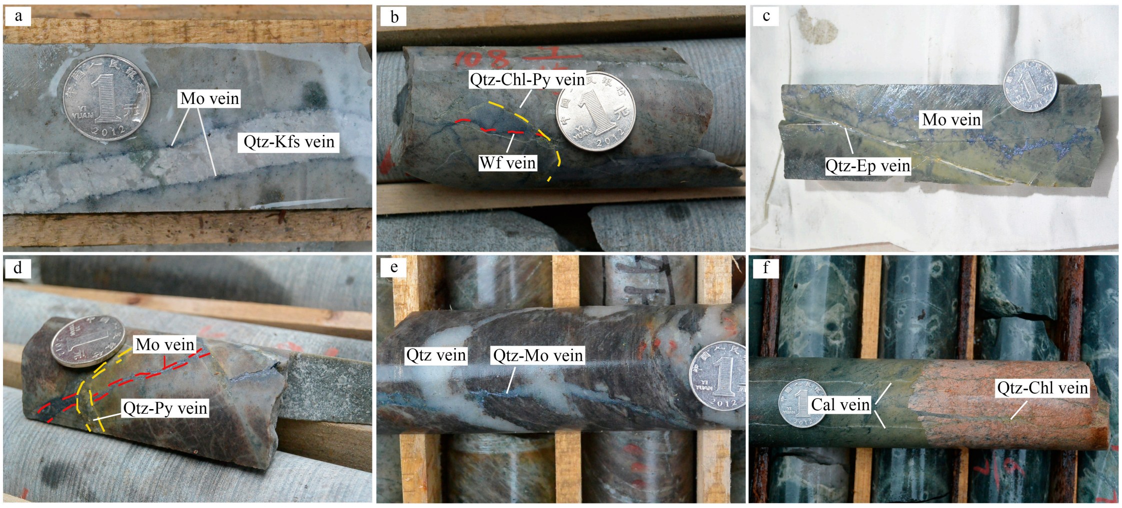

Figure 4. Photographs showing various veins in the Langcun deposit. (**a**) Quartz–molybdenite vein in the aplite of stage I; (**b**) early wolframite vein cut by the quartz–chlorite–pyrite vein in stage III; (**c**) molybdenite vein cut by the quartz–epidote vein in stage III; (**d**) molybdenite vein cut by the quartz–pyrite vein in stage III; (**e**) quartz–molybdenite vein cut by the quartz vein in stage III; (**f**) quartz–chlorite vein cut by the calcite in stage IV. Abbreviations: Cal—calcite; Ep—epidote; Chl—chlorite; Kfs—K-feldspar; Py—pyrite; Qtz—quartz; Mo—molybdenite; Wf—wolframite.

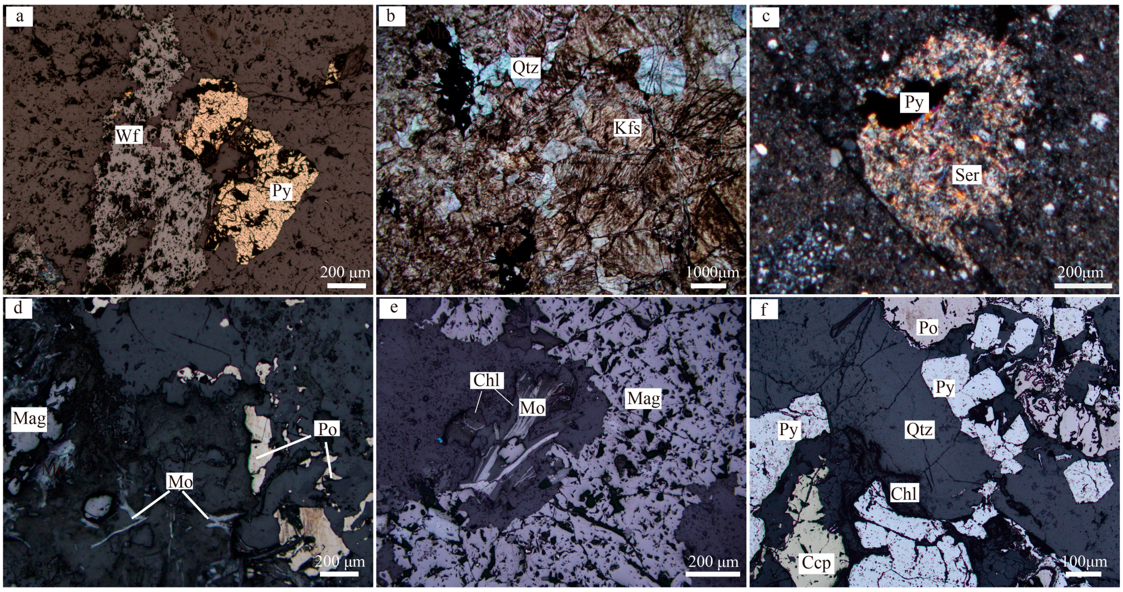

Figure 5. Photomicrographs of ores in the Langcun deposit. (**a**) Wolframite coexisting with pyrite in stage I; (**b**) molybdenite occurring in quartz–K-feldspar druses; (**c**) pyrite occurring in stage II; (**d**) molybdenite coexisting with magnetite and pyrrhotite in stage II; (**e**) molybdenite and magnetite occurring with chlorite in stage III; (**f**) pyrite, pyrrhotite, and chalcopyrite in stage III. Abbreviations: Chl—chlorite; Ccp—chalcopyrite; Kfs—K-feldspar; Po—pyrrhotite; Py—pyrite; Qtz—quartz; Mag—magnetite; Mo—molybdenite; Ser—sericite; Wf—wolframite.

Stage III: Quartz–chlorite–pyrite stage.

Granitic wall rocks are pervasively altered by chlorite, quartz sulfide, and quartz–chlorite (pyrite) veins, which together with barren quartz veins crosscut older wolframite veins (Figure 4b), molybdenite veins (Figure 4c,d), and quartz–molybdenite veins (Figure 4e). The mineral assemblage of this stage includes quartz, chlorite, pyrite with minor molybdenite sphalerite, and galena (Figure 5e,f).

Stage IV: Calcite stage.

Extensive carbonation and calcite veins over country rocks characterize this stage—these carbonate veins crosscut quartz–chlorite veins (Figure 4f), with the mineral assemblage dominated by calcite with little quartz and chlorite.

3. Samples and Analytical Methods

Samples for fluid inclusion studies were carefully collected across all mineralization stages. These samples, mostly quartz and calcite veins, were prepared as double-polished thin sections (~300 μm thick) for further observation and tests.

The microthermometric study was conducted in the Fluid Inclusion Laboratory at the University of Science and Technology Beijing, Beijing, China (USTB), using a Linkam THMS600 heating–freezing stage with a temperature range from −196 °C to 600 °C. The accuracy of the temperature measurement was within ±0.2 °C for temperatures below 30 °C, ±0.1 °C for the interval between 30 and 100 °C, and approximately ±2 °C from 100 to 600 °C. The heating rate was initially set at 1–20 °C/min for the early stages of each run and was reduced to 0.3–1 °C/min as the samples approached the phase change point.

The compositions of individual fluid inclusions were identified using HORIBA Jobin Yvon HR800-type laser Raman spectroscopy with a laser wavelength of 633 nm in the Inclusion Analysis Laboratory at the Beijing Research Institute of Uranium Geology, Beijing, China (BRIUG). The scanning band was set to 1000–4000 cm^{-1} with a buildup time of 1 min for each scan. The spectral resolution was ±0.14 cm^{-1} with a beam size of 2 μm.

Scanning electron microscopy/X-Ray Energy Dispersive Spectrum (SEM/EDS) analysis of daughter minerals in the fluid inclusions was performed at the Fluid Inclusion Laboratory, USTB, using Phenom XL SEM equipped with an energy dispersive spectrometer (EDS) system and element identification software. The accelerating voltage was 15 kV, with a resolution of 10 nm and a maximum magnification of 100,000×. The samples used in the experiment were prepared using a natural opening method for fluid inclusions. The samples were crushed to yield particles 3 to 5 mm in size. Particles with relatively flat cross-sections were selected and mounted on a glass slide with their flat surfaces facing upward for observation.

Typical quartz samples from the first three stages were selected for H-O and S isotopic analyses at BRIUG. The samples were processed using the BrF_5 method described by Clayton and Mayeda [27], and then the O-isotopic composition was determined using a MAT-253 mass spectrometer. All values are reported relative to the V-SMOW standard [28], with an uncertainty of ±0.2‰. H isotope analyses were conducted on the same samples using the Zn reduction method at 450 °C [29]. Measurements were performed by the MAT-252EM instrument, with analytical precision for δD of ±2‰. Thirteen pyrite and molybdenite samples were used for the sulfur isotope analysis. The method of SO_2 extraction was described by Robinson and Kusakabe [30]; the S isotopic ratio ($^{34}S/^{32}S$) was measured on the Finnigan MAT-251 mass spectrometer with a precision of ±0.2‰.

4. Results

4.1. Fluid Inclusion Petrography

Through the phase composition of fluid inclusion at room temperature and the phase transition characteristics during heating and cooling [31], primary fluid inclusions were classified into four types: two-phase liquid-rich fluid inclusions (type LV), three-phase CO_2-rich fluid inclusions (type LC), pure CO_2 fluid inclusions (type C), and multi-phase inclusions with daughter minerals (type LDV).

Type-LV inclusion has a negative crystal, ellipsoidal, and irregular form, and consists of an aqueous liquid and vapor phase (Figure 6a) with a vapor volume percentage ranging from 12% to 45%.

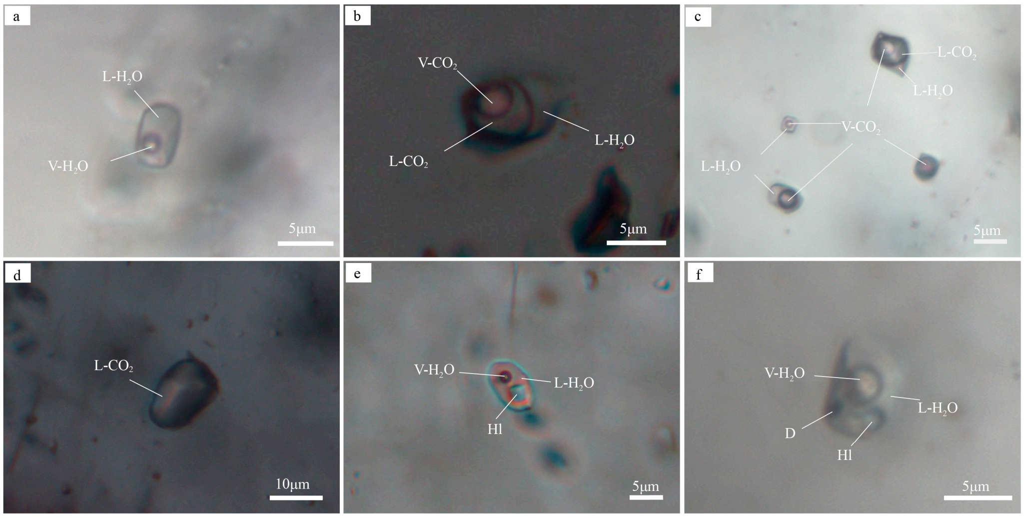

Figure 6. Microphotographs showing different types of fluid inclusions at the Langcun W-Mo deposit. (**a**) Type-LV inclusion; (**b**) type-LC inclusion containing three phases (L_{H2O} + L_{CO2} + V_{CO2}); (**c**) type-LC inclusions with various filling percentages; (**d**) type-C inclusion; (**e**) type-LDV inclusion with a halite daughter mineral; (**f**) type-LDV inclusion with multiple daughter minerals. Abbreviations: Hl—halite.

Type-LC inclusion has liquid H_2O, liquid CO_2, and vapor CO_2 (Figure 6b,c); only liquid H_2O and vapor CO_2 are partially seen at room temperature (Figure 6c) and CO_2 liquid circles appear during cooling. Type-LC inclusions are mainly negative crystal and ellipsoidal in shape, 5–9 μm in size, and have gas phase filling in the range of 20%–80%, and such inclusions are developed in stages I and II.

Type-C inclusion contains little to no water with high CO_2 phase volumetric proportions ($V_{CO2} > 90\%$) (Figure 6e). It is generally 5–15 μm in size and has a sub-circular or elliptical shape, often in close association with LC-type inclusions. Type-C inclusion is mainly seen in stages I and II.

Type-LDV inclusions comprise an aqueous liquid, a vapor, and one or multiple daughter minerals (Figure 6e,f). Type-LDV inclusions are mostly isolated, with a negative crystalline or irregular shape, and 6–15 μm in size. Transparent daughter minerals are mainly halite, while opaque daughter minerals can be recognized as chalcopyrite (see Section 4.4). This type of inclusion occurs primarily in an early stage.

4.2. Microthermometry of Fluid Inclusion

The microthermometry results of fluid inclusions are summarized in Table 1 and Figure 7.

Table 1. Summary of fluid inclusion data from the Langcun deposit.

Host Mineral	Mineralized Stage	Inclusion Type	$T_{m, CO2}$	$T_{m, ice}$	$T_{m, clath}$	$T_{h, CO2}$	$T_{h, total}$	$T_{m, halite}$	Salinity
			°C	°C	°C	°C	°C	°C	wt.% NaCl
Quartz	I	LDV					281~312	362~392	43.5~46.6
		LC	−58.0~−57.0		3.3~7.9	20.8~30.5	296~377		3.95~11.57
		C	−58.1~−57.0			27.7~31.1			
		LV		−6.0~−1.1			287~387		1.74~9.21

Table 1. *Cont.*

Host Mineral	Mineralized Stage	Inclusion Type	$T_{m,\ CO2}$	$T_{m,\ ice}$	$T_{m,\ clath}$	$T_{h,\ CO2}$	$T_{h,\ total}$	$T_{m,\ halite}$	Salinity
			°C	°C	°C	°C	°C	°C	wt.% NaCl
Quartz	II	LC	−58.3~−57.6		7.5~8.6	26.9~30.2	228~342		2.77~5.14
		C	−58.4~−57.6			25.2~28.9			
Quartz	III	LV		−3.3~−1.0			224~275		1.74~4.96
Calcite	IV	LV		−2.4~−0.6			200~225		1.06~3.39

The pressure correction for LV inclusions has not been conducted.

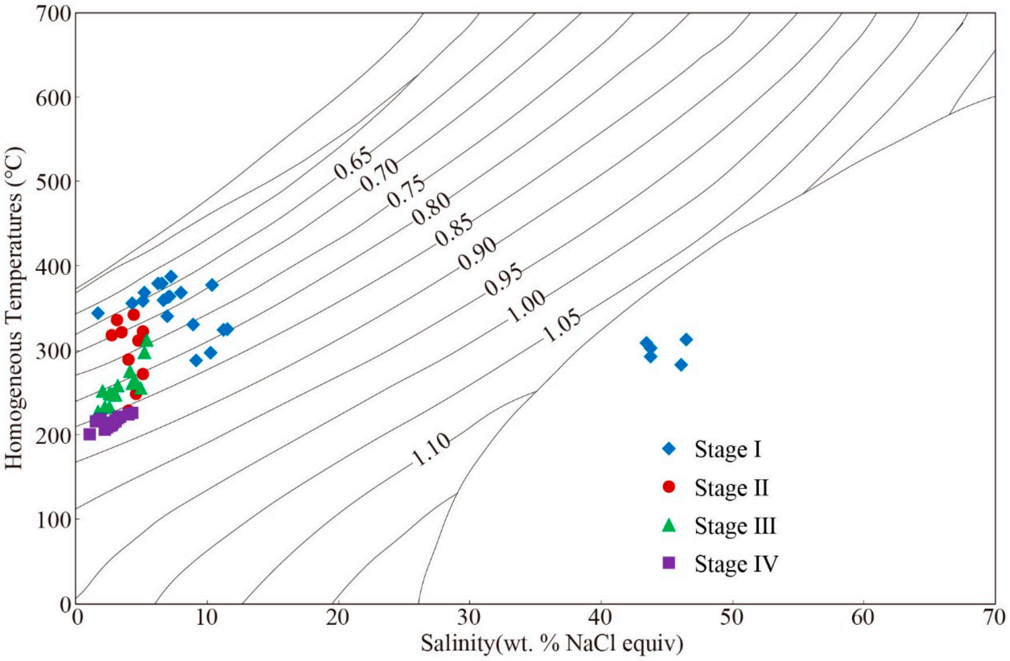

Figure 7. Salinity vs. homogenization temperatures of fluid inclusions in the Langcun W-Mo deposit.

Stage I contains type-LV, -LC, -C, and -LDV fluid inclusions, which often have a close spatial association, showing the characteristics of non-homogeneous capture. Halite daughter minerals disappear later than vapor in type-LDV inclusions during the heating process, with melting temperatures of 362~392 °C and salinities of 43.5~46.6 wt.% NaCl equiv. Type-LV inclusions yielded ice-melting temperatures (Tm_{ice}) of −6.0~−1.1 °C and salinities of 1.74~9.21 wt.% NaCl equiv with homogenization temperatures (Th_{total}) between 287 and 387 °C. Type-LC inclusion temperatures of CO_2 solid melting (Tm_{CO2}) are between −58.0 and 57.0 °C; the melting temperatures of clathrate (Tm_{clath}) range from 3.3 to 7.9 °C, with calculated salinities between 3.95 and 11.57 wt.% NaCl equiv (Collins, 1979). The temperatures of partial homogenization (Th_{CO2}) for CO_2 phases range from 20.8 to 30.5 °C with CO_2 liquid disappearance. Th_{total} for type LC range from 296 to 377 °C, with final homogenization generally occurring in the liquid phase. Tm_{CO2} for type C is between −58.1 and −57.0 °C, and Th_{CO2} is between 27.7 and 31.1 °C.

The main types of fluid inclusions in stage II are types LC and C. Tm_{CO2} is between −58.3 and −57.6 °C, Tm_{clath} ranges from 7.5 to 8.6 °C, and the corresponding calculated salinities are 2.77~5.14 wt.% NaCl equiv. Th_{CO2} and Th_{total} for type LC are 26.9~30.2 °C and 228~342 °C, respectively. Tm_{CO2} for type C is between −58.4 and −57.6 °C, and Th_{CO2} is between 25.2 and 28.9 °C.

Stages III and IV are mainly type-LV inclusions. Stage III showed that Tm_{ice} ranged from −3.3 to −1.0 °C, with calculated salinities of 1.74 and 4.96 wt.% NaCl equiv, and Th_{total} between 224 and 275 °C, which mainly occurs in the liquid phase. Type-LV inclusions in stage IV have Tm_{ice} values ranging from −2.4 to −0.6 °C, with calculated salinities ranging from 1.06 to 3.39 wt.% NaCl equiv, and Th_{total} ranging from 200 to 225 °C, mainly in the liquid phase.

4.3. Laser Raman Spectroscopy Analysis

Representative FIs were measured using Laser Raman microspectroscopy to constrain their compositions. The results show that the vapor and liquid phases of the LV- and LDV-type inclusions are dominated by H_2O (Figure 8a–d). The vapor phase of the LC- and C-type inclusions is dominated by CO_2 (1284.82 cm^{-1} and 1388.53 cm^{-1}, respectively, Figure 8e,g) with a small amount of N_2 (2915.73 cm^{-1}, Figure 8f) and CH_4 (2915.73 cm^{-1}, Figure 8h). The vapor and liquid phases of inclusion in stage III are all H_2O (Figure 8i,j).

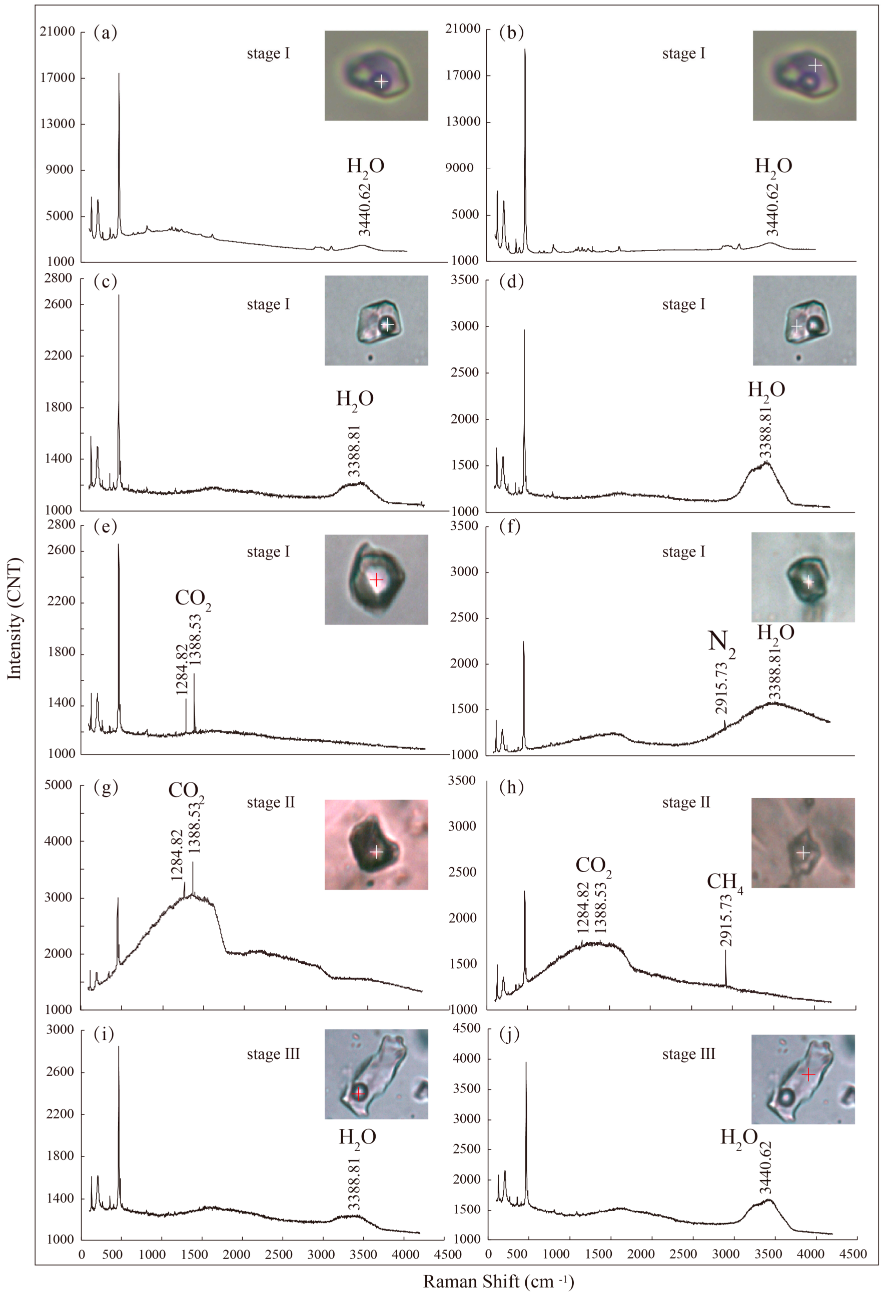

Figure 8. Representative Raman spectra of fluid inclusions in quartz. (**a**,**b**) H_2O spectra of the vapor phase and liquid phase in the type-LDV inclusion of stage I; (**c**,**d**) H_2O spectra of the vapor phase and

liquid phase in the type-LV inclusion of stage I; (**e**) CO_2 spectrum of the vapor phase in the type-C inclusion of stage I; (**f**) H_2O and N_2 spectra of the vapor phase in the type-LC inclusion of stage I; (**g**) CO_2 spectrum of the vapor phase in the type-C inclusion of stage II; (**h**) CO_2 and CH_4 spectra of the vapor phase in the type-LC inclusion of stage II; (**i**,**j**) H_2O spectra of the vapor phase and liquid phase in the type-LV inclusion of stage III. "+" indicates the focus of Raman laser beam.

4.4. SEM Analysis of Daughter Minerals

The petrographic observation shows that the daughter minerals in type-LDV inclusions at the early stage are both transparent and opaque. SEM analysis results reveal that the daughter minerals include the following: (1) halite, which can occur alone or coexist with other daughter minerals (Figure 9a–c); (2) strontianite, as shown by peaks of C, O, and Sr in the SEM/EDS energy spectrum (Figure 9d), which is columnar in shape, and often coexists with halite in fluid inclusions; (3) ilmenite, occurring in fluid inclusions of rutile (Figure 9e), characterized by peaks of O, Fe, and Ti in the energy spectrum (Figure 9f); (4) sericite, which is flake-like in shape (Figure 9g) and contains O, Si, Al, and K with an Al/K atomic ratio of about 3:1 (Figure 9h), and is more common in the early stage and often co-occurs with other daughter minerals, such as calcite (Figure 9g,i), chalcopyrite (Figure 9j), and pyrite; (5) chalcopyrite, with a tetrahedral shape and peaks of S, Cu, and Fe in the energy spectrum (Figure 9k), which can coexist with sericite and rhodochrosite (Figure 9l); and (6) pyrite, characterized by its cubic shape (Figure 9m) and Fe and S in the X-ray map analysis.

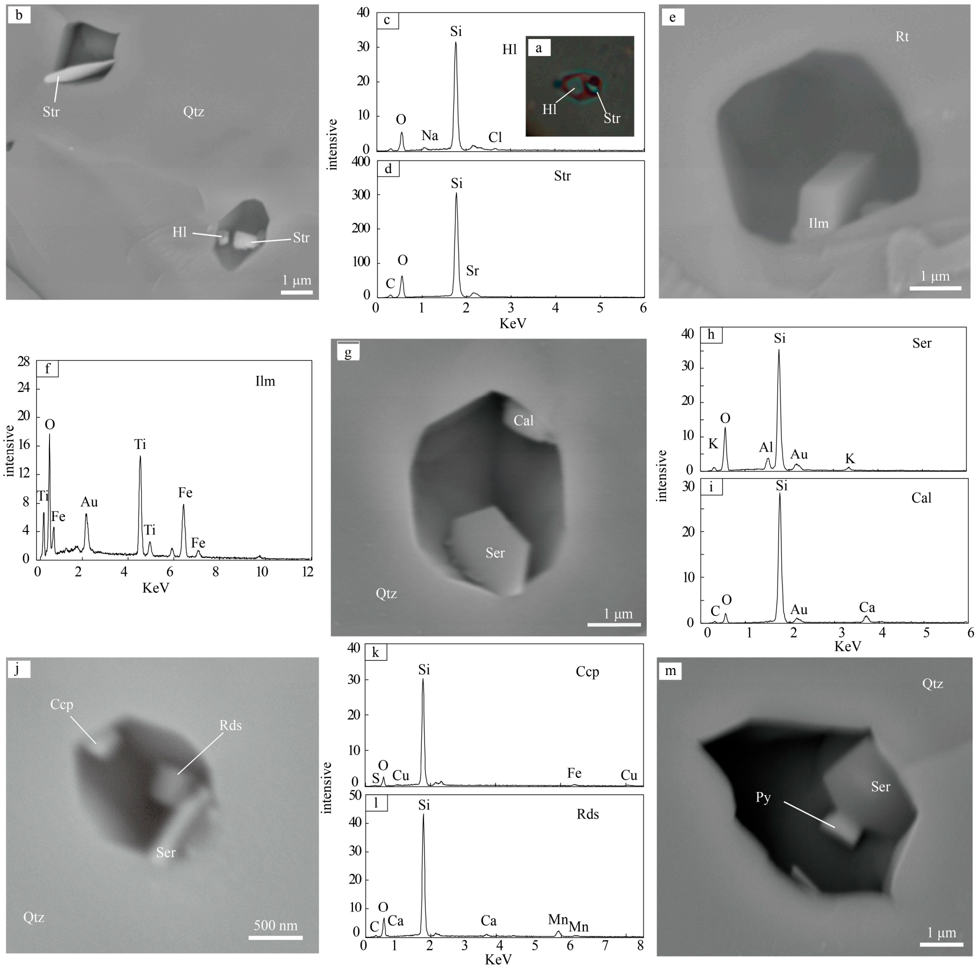

Figure 9. Backscattered electron images and X-ray spectrum of daughter minerals in inclusions. (**a**,**b**) Microphotograph and backscattered electron images of halite and strontianite in inclusions,

respectively; (**c**,**d**) X-ray spectra of halite and strontianite, respectively; (**e**,**f**) backscattered electron image and X-ray spectrum of ilmenite in fluid inclusions of rutile; (**g**) backscattered electron images of sericite and calcite in inclusions; (**h**,**i**) X-ray spectra of sericite and calcite, respectively; (**j**) backscattered electron images of chalcopyrite, sericite, and rhodochrosite in inclusions; (**k**,**l**) X-ray spectra of chalcopyrite and rhodochrosite, respectively; (**m**) backscattered electron image of pyrite. Abbreviations: Cal—calcite; Ccp—chalcopyrite; Hl—halite; Ilm—ilmenite; Py—pyrite; Qtz—quartz; Rds—rhodochrosite; Rt—rutile; Ser—sericite; Str—strontianite.

All of the abovementioned daughter minerals were precipitated from the fluid after trapping. The evidence supporting this conclusion is multifaceted: (1) the daughter minerals exhibit regular crystal forms within the inclusions and have a growth relationship with the inclusions; (2) the presence of daughter minerals is exclusively observed within the primary inclusions of stage I, and the recurrence of identical daughter minerals is noted; and (3) minerals that correspond to the daughter minerals also develop within aplite and granite porphyry.

4.5. H-O Isotopic Compositions

The hydrogen and oxygen isotopic compositions of the analyzed quartz samples are presented in Table 2 and Figure 10. The δD values of the extracted water for quartz in stage I range from −70.4% to −89.0%. The δD values of quartz from stage II and III range from −68.5% to −76.9% and −80.5% to −85.1%, respectively. The measured $\delta^{18}O$ value of quartz from stage I ranges from 9.4‰ to 12.8‰. Using the equations of Matsuhisa [32] and the corresponding fluid inclusion average homogenization temperature data, the $\delta^{18}O$ value of aqueous fluid from stage I was calculated to range from 3.8‰ to 7.2‰. The $\delta^{18}O$ value of quartz from stages II and III range from 9.0‰ to 9.6‰ and 6.5‰ to 11.3‰, respectively, and the calculated $\delta^{18}O$ values of fluid range from 2.0‰ to 2.6‰ and −2.9‰ to 1.9‰, respectively.

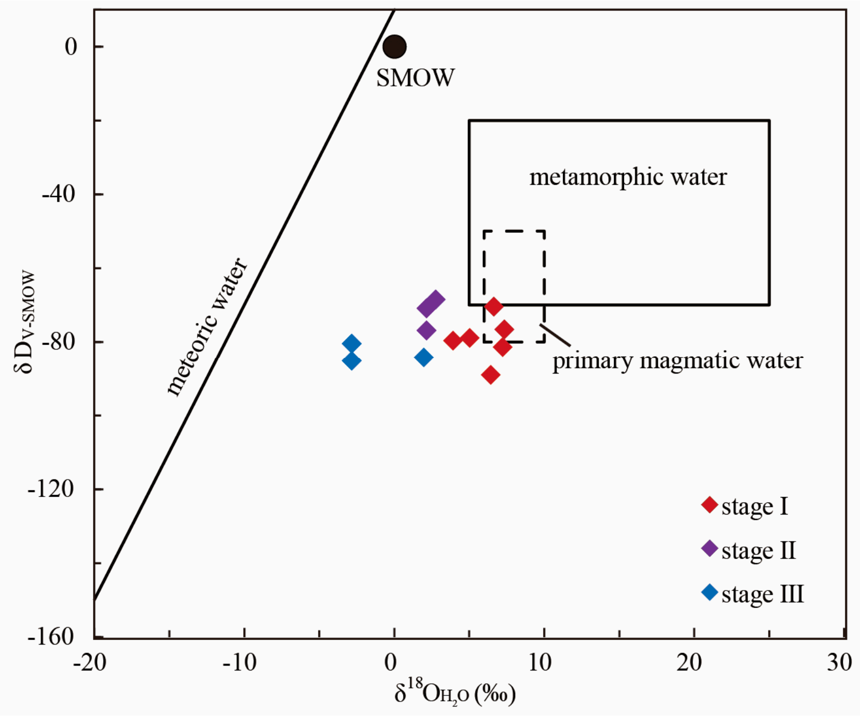

Figure 10. $\delta^{18}O_{H2O}$ vs. δD diagram of the Langcun W-Mo deposit (base map after [33]).

Table 2. Oxygen and hydrogen isotopic data for quartz from the Langcun W-Mo deposit.

Sample Number	Mineral	Ore-Formation Stage	$\delta D_{V\text{-}SMOW}$ (‰)	δ^{18} $O_{V\text{-}SMOW}$ (‰)	$\delta^{18}O_{H2O}$ (‰)
LC1064	Quartz	I	−78.9	10.5	4.9
LC2018	Quartz		−79.6	9.4	3.8
LC1058	Quartz		−89.0	11.9	6.3
LC1036	Quartz		−81.4	12.7	7.1
LC2044	Quartz		−76.6	12.8	7.2
LC2035	Quartz		−70.4	12.1	6.5
LC2020	Quartz	II	−68.5	9.6	2.6
LC2034	Quartz		−70.9	9	2.0
LC2021	Quartz		−76.9	9	2.0
LC1093	Quartz	III	−80.5	6.5	−2.9
LC1013	Quartz		−85.1	6.5	−2.9
LC1078	Quartz		−84.2	11.3	1.9

4.6. Sulfide S Isotopic Compositions

The S isotope results are shown in Table 3. The δ^{34}S values in pyrite and molybdenite range from 5.7‰ to 9.5‰ and 4.2‰ to 7.2‰, respectively, and are mostly concentrated in the range of 7‰ to 8‰.

Table 3. S isotope of sulfide from the Langcun W-Mo deposit.

Sample Number	Ore-Formation Stage	Mineral	δ^{34}S $_{V\text{-}CDT}$‰
LC1064	I	Pyrite	7.1
LC2018		Pyrite	6.7
LC2035		Pyrite	6.3
LC2044		Pyrite	7.1
LC2043		Pyrite	5.7
LC1047	II	Pyrite	5.7
LC1070		Molybdenite	7.2
LC2021		Molybdenite	4.2
LC1093		Pyrite	8.3
LC1026	III	Pyrite	6.8
LC1046		Pyrite	9.5
LC1078		Pyrite	7.6
LC2033		Pyrite	9.3

5. Discussion

5.1. Source of the Ore-Forming Material

Because of the absence of sulfates, we assume that the sulfur isotopic composition of these sulfides can be considered as representative of the overall sulfur isotope signature of the Langcun deposit. The sulfur isotopes exhibit a narrow range from 4.2‰ to 9.5‰, clustering between 7.0‰ and 8.0‰ (Figure 11), and a variation not exceeding 5‰, slightly higher than the typical δ^{34}S values of mantle sources [34], indicating that the sulfides in the mineralization stage were mixed with heavy sulfur isotopes.

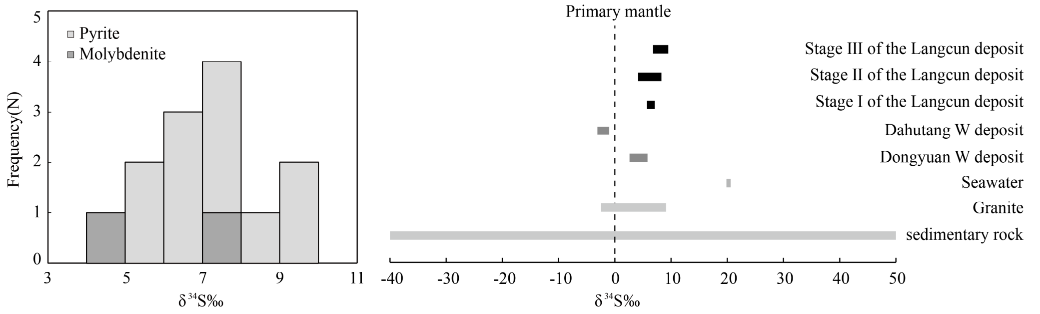

Figure 11. Frequency histogram and distribution of δ^{34}S from the Langcun W-Mo deposit.

Typically, the sulfur isotopic composition of primitive mantle is relatively homogeneous, with $\delta^{34}S$ values ranging from 0 to 3‰. Magmatic sources generally have $\delta^{34}S$ values near 0‰, rarely exceeding 8‰. In contrast, sedimentary rocks exhibit a broader isotopic variation, spanning from −40‰ to 50‰ [34]. Compared to the S natural reservoir, most of the $\delta^{34}S$ values in the Langcun W-Mo deposit are close to the magmatic sulfur source. Moreover, the $\delta^{34}S$ value at the early stage is slightly lower than that at the late stage in the Langcun deposit (Figure 11) and is higher than that of magmatic sulfur-source W deposits in South China, such as the Dongyuan W-Mo deposit [35] and Dahutang W deposit [36]. Higher $\delta^{34}S$ values can be explained by the incorporation of some sedimentary sulfur through the interaction with sedimentary rocks [37].

5.2. Magmatic Fluid Evolution

Magmatic fluid exsolution is a pivotal process in magmatic–hydrothermal systems, which can transport a significant amount of metallic elements, thereby contributing to the formation of polymetallic deposits [38,39]. In the Langcun deposit, the mineralization of wolframite and molybdenite is intricately linked to granitic porphyry and aplite. The presence of quartz–K-feldspar druses and early quartz–K-feldspar veins within the aplite illustrate the magmatic fluid exsolution process. The aplite structure and the quartz–K-feldspar druses within aplite imply that decompression boiling (first boiling), triggered by the rapid ascent of magma, is likely the predominant mechanism of fluid exsolution.

The fluid inclusions study in stage I reveals a variety of inclusions with different vapor–liquid ratios and halite daughter minerals assemblage. Notably, liquid- and vapor-rich inclusions show different homogenization patterns during heating, with the former homogenizing to the liquid phase and the latter homogenizing to the vapor phase. On the other hand, the range of homogenization temperatures is similar, indicative of boiling fluid inclusions assemblage. This suggests that fluid boiling is a key process in the early stage of mineralization. Fluid boiling leads to phase separation, forming a high-salinity liquid-rich phase and a low-salinity CO_2-rich phase fluid. The results of the fluid inclusion studies indicate that early magmatic exsolution fluid belongs to the NaCl-H_2O-CO_2 system with a high temperature (~387 °C) and high–medium salinity (1.74–46.60 wt.% NaCl equiv). H-O isotope analysis shows that the δD values and calculated $\delta^{18}O$ values overlap near the primary magmatic fluids [33], implying that the ore-forming fluids are dominantly magmatic. In contrast, the isotopic data of fluids for stages III and IV show low $\delta^{18}O$ values, and the plots in the $\delta^{18}O_{H2O}$ versus δD_{H2O} diagram (Figure 10) indicate a significant influence of meteoric water, which is consistent with the fluid characterized by the low temperature and low salinity in late stages. Therefore, we suggest that the primary ore-forming fluids were derived from the magmatic exsolution and were predominantly of magmatic origin, whereas stages III and IV had the contribution of meteoric water.

5.3. Ore-Forming Mechanisms

The transport and precipitation of W in hydrothermal fluids involve complex mechanism. Wood and Samson [40] concluded through thermodynamic experiments that, under certain temperature and pressure conditions, tungsten migrates mainly as simple tungstic acid (WO_4^{2-}, H_2 WO_4, HWO_4^-, and $KHWO_4$) and basic tungstate ion pairs (KWO_4^-, $NaWO_4^-$, and $NaHWO_4$) in the hydrothermal fluid of the NaCl-H_2O-CO_2 composition. The main mechanisms of tungsten precipitation include (1) the natural cooling of the fluid [41]; (2) a water–rock reaction [42,43]; (3) fluid immiscibility/boiling [44]; and (4) fluid mixing [45,46]. The role of CO_2 in W mineralization is still a contentious issue. Ni et al. [41] suggested the minor role that CO_2 plays in tungsten mineralization, given the absence of CO_2-bearing inclusions in wolframite. However, several studies have documented variable

CO_2 contents in the ore-forming fluids of W and Mo deposits, such as the Dajishan W deposit, Xingluokeng W deposit [47], and Larong W-Mo deposit in Tibet [48]. The presence of CO_2 may be a common feature of ore-forming fluids of W and Mo deposits [49]. Higgins [50] suggested that, under high-temperature conditions, tungsten in CO_2-rich fluids may migrate as carbonates and bicarbonates. CO_2 escape causes the pH fluctuation in the fluid and disrupts the tungsten complex equilibrium, which in turn causes the precipitation of W minerals [47,48]. Through the calculation of the reaction equilibrium model, Liu and Zhang [51] concluded that CO_2 escape can reduce tungsten solubility in the fluid, promoting the precipitation of wolframite.

Microthermometry results show that the temperature from stages I to II does not decrease significantly, and there is no clear evidence of fluid mixing. However, wolframite predominantly precipitated during stage I, indicating that cooling and fluid mixing were not the primary drivers of precipitation for wolframite in the Langcun deposit. As described above, fluid boiling occurred in the early stage of mineralization, which likely reduced the stability of metal complexes in the fluid system and may have been a critical factor for wolframite mineralization. Although some molybdenite was present in the early stages, the main mineralization occurred later than that of wolframite. H-O isotopes suggest a minor addition of meteoric water to the fluid during stage II. In addition, the absence of CO_2-bearing inclusions in stage III implies that CO_2 escape occurred during or before that stage (Figure 12). A significant number of CO_2-rich fluid inclusions developed during the early stages of W-Mo mineralization, especially in quartz associated with W-Mo mineralization, whereas such inclusions are rarely seen in the late stages. This suggests that CO_2 escaping during the main mineralization stages could have triggered the precipitation of wolframite and molybdenite. Therefore, CO_2 appears to be a favorable factor for W-Mo mineralization. In summary, fluid mixing and CO_2 escape could be the primary mechanisms for Mo mineralization in the Langcun deposit.

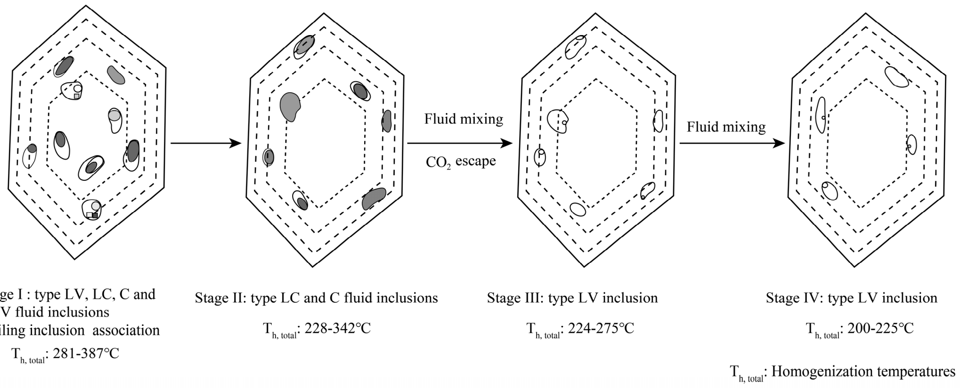

Figure 12. Diagram of the fluid evolution process in the Langcun W-Mo deposit.

6. Conclusions

1. The Langcun W-Mo deposit is a porphyry deposit that has evolved through four stages: quartz–K-feldspar of stage I, quartz–sericite–molybdenite of stage II, quartz–chlorite–pyrite of stage III, and calcite of stage IV. Among these, stages I and II are the main mineralization stages. The fluid inclusions encompass a variety of types: two-phase liquid-rich fluid inclusions (type LV), three-phase CO_2-rich fluid inclusions (type LC), pure CO_2 fluid inclusions (type C), and multi-phase inclusions with daughter minerals (type LDV).

2. The primary ore-forming fluids stem from magmatic exsolution, exhibiting high–moderate temperatures, high–moderate salinity, and are rich in CO_2. The H-O isotope data indicate that the ore-forming fluids are predominately magmatic in origin, which,

however, during the later stage of mineralization, were mixed with meteoric water, leading to the decrease in the temperature and salinity of ore-forming fluids.

3. Early W-Mo precipitation was triggered by fluid boiling. The escape of CO_2, coupled with the mixing of magmatic fluid with meteoric water, facilitated the precipitation of molybdenite.

Author Contributions: Data curation, K.C.; funding acquisition, Y.X.; investigation, K.C., Y.Q. and K.Y.; project administration, Y.X.; resources, Y.X.; supervision, Y.X. and Z.H.; writing—original draft, K.C.; writing—review and editing, Y.Q. All authors have read and agreed to the published version of the manuscript.

Funding: This research was funded by the 12th Five–Year Plan project of the National Science & Technology Pillar Program, grant number 2011BAB04B00, and the public welfare industry fund of the Ministry of Land and Resources, grant number 20101101.

Data Availability Statement: Data are contained within the article.

Acknowledgments: Many thanks to Qi Chen for his help with the fieldwork and Hao Cui for his help with the laser Raman spectroscopy analysis.

Conflicts of Interest: Kejun Yang is an employee of Jiangxi Copper (Hong Kong) Investment Co., Ltd. The paper reflects the views of the scientists and not the company.

References

1. Sheng, J.F.; Liu, L.J.; Wang, D.H.; Chen, Z.H.; Ying, L.J.; Huang, F.; Wang, J.H.; Zeng, Q. A preliminary review of metallogenic regularity of tungsten deposits in China. *Acta Geol. Sin. (Eng. Ed.)* **2015**, *89*, 1359–1374. [CrossRef]
2. Zhao, W.W.; Zhou, M.F.; Li, Y.H.M.; Zhao, Z.; Gao, J.F. Genetic types, mineralization styles, and geodynamic settings of Mesozoic tungsten deposits in South China. *J. Asian Earth Sci.* **2017**, *137*, 109–140. [CrossRef]
3. Ni, P.; Pan, J.Y.; Han, L.; Cui, J.M.; Gao, Y.; Fan, M.S.; Li, W.S.; Chi, Z.; Zhang, K.H.; Cheng, Z.L.; et al. Tungsten and tin deposits in South China: Temporal and spatial distribution, metallogenic models and prospecting directions. *Ore Geol. Rev.* **2023**, *157*, 105453. [CrossRef]
4. Zhao, Z.; Fu, T.Y.; Gan, J.W.; Liu, C.; Wang, D.H.; Sheng, J.F.; Li, W.B.; Wang, P.A.; Yu, Z.F.; Chen, Y.C. A synthesis of mineralization style and regional distribution and a proposed new metallogenic model of Mesozoic W-dominated polymentallic deposits in South China. *Ore Geol. Rev.* **2021**, *133*, 104008. [CrossRef]
5. Jiang, W.C.; Li, H.; Mathur, R.; Wu, J.H. Genesis of the giant Shizhuyuan W–Sn–Mo–Bi–Pb–Zn polymetallic deposit, South China: Constraints from zircon geochronology and geochemistry in skarns. *Ore Geol. Rev.* **2019**, *111*, 102980. [CrossRef]
6. Feng, C.Y.; Huang, F.; Zeng, Z.L.; Qu, W.J.; Ding, M. Isotopic chronology of Jiulongnao granite and Hongshuizhai greisens-type tungsten deposit in South Jiangxi Province. *J. Jilin Univ. (Earth Sci. Ed.)* **2011**, *41*, 112–121. (In Chinese with English Abstract) [CrossRef]
7. Mao, J.W.; Xiong, B.K.; Liu, J.; Pirajno, F.; Cheng, Y.B.; Ye, H.S.; Song, S.W.; Dai, P. Molybdenite Re/Os dating, zircon U-Pb age and geochemistry of granitoids in the Yangchuling porphyry W-Mo deposit (Jiangnan tungsten ore belt), China: Implications for petrogenesis, mineralization and geodynamic setting. *Lithos* **2017**, *286–287*, 35–52. [CrossRef]
8. Mao, Z.H.; Liu, J.J.; Mao, J.W.; Deng, J.; Zhang, F.; Meng, X.Y.; Xiong, B.K.; Xiang, X.K.; Luo, X.H. Geochronology and geochemistry of granitoids related to the giant Dahutang tungsten deposit, middle Yangtze River region, China: Implications for petrogenesis, geodynamic setting, and mineralization. *Gondwana Res.* **2015**, *28*, 816–836. [CrossRef]
9. Qin, Y.; Wang, D.H.; Wu, L.B.; Wang, K.Y.; Mei, Y.P. Zircon SHRIMP U-Pb dating of the mineralized porphyry in the Dongyuan W deposit in Anhui province and its geological significance. *Acta Geol. Sin.* **2010**, *84*, 479–484. (In Chinese with English Abstract) [CrossRef]
10. Zhang, J.J.; Chen, Z.H.; Wang, D.H.; Chen, Z.Y.; Liu, S.B.; Wang, C.H. Geological characteristics and metallogenic epoch of the Xingluokeng tungsten deposit, Fujian province. *Geotecton. Metallog.* **2008**, *32*, 92–97. (In Chinese with English Abstract) [CrossRef]
11. Shu, L.S.; Charvet, J. Kinematic and geochronology of the Proterozoic Dongxiang–Shexian ductile shear zone: With HP metamorphism and ophiolitic melange (Jiangnan Region, South China). *Tectonophysics* **1996**, *267*, 291–302. [CrossRef]
12. Li, X.H.; Li, Z.X.; Zhou, H.; Liu, Y.; Kinny, P.D. U-Pb zircon geochronology, geochemistry and Nd isotopic study of Neoproterozoic bimodal volcanic rocks in the Kangdian Rift of South China: Implications for the initial rifting of Rodinia. *Precambrian Res.* **2002**, *113*, 135–154. [CrossRef]

13. Li, Z.X.; Li, X.H.; Zhou, H.W.; Kinny, P.D. Grenvillian continental collision in south China: New SHRIMP U–Pb zircon results and implications for the configuration of Rodinia. *Geology* **2002**, *2*, 163–166. [CrossRef]
14. Li, X.H. Cretaceous magmatism and lithospheric extension in Southeast China. *J. Asian Earth Sci.* **2000**, *18*, 293–305. [CrossRef]
15. Zhou, X.M.; Sun, T.; Shen, W.Z.; Shu, L.S.; Niu, Y.L. Petrogenesis of Mesozoic granitoids and volcanic rocks in South China: A response to tectonic evolution. *Episodes* **2006**, *29*, 25–33. [CrossRef]
16. Li, Z.X.; Li, X.H. Formation of the 1300-km-wide intracontinental orogen and postorogenic magmatic province in Mesozoic South China: A flat–slab subduction model. *Geology* **2007**, *35*, 179–182. [CrossRef]
17. Hua, R.M.; Chen, P.R.; Zhang, W.L.; Liu, X.D.; Lu, J.J.; Lin, J.F.; Yao, J.M. Preliminary study on Mesozoic and Cenozoic ore-forming systems related to granitic magmatism South China. *Miner. Depos.* **2005**, *21*, 132–135. (In Chinese with English Abstract) [CrossRef]
18. Mao, J.W.; Xie, G.Q.; Li, X.F. Mesozoic large-scale mineralization and multiple lithospheric extensions from South China. *Earth Sci. Front.* **2004**, *11*, 45–56. (In Chinese with English Abstract) [CrossRef]
19. Li, X.H.; Li, Z.X.; Li, W.X.; Liu, Y.; Yuan, C.; Wei, G.J.; Qi, C.S. U-Pb zircon geochemical and Sr-Nd-Hf isotopic constraints on age and origin of Jurassic I- and A-type granites from central Guangdong, SE China: A major igneous event in response to foundering of a subducted flat–slab? *Lithos* **2007**, *96*, 186–204. [CrossRef]
20. Wong, J.; Sun, M.; Xing, G.F.; Li, X.H.; Zhao, G.C.; Wong, K.; Yuan, C.; Xia, X.P.; Li, L.M.; Wu, F.Y. Geochemical and zircon U-Pb and Hf isotopic study of the Baijuhuajian metaluminous A–type granite: Extension at 125–100? Ma and its tectonic significance for South China. *Lithos* **2009**, *112*, 289–305. [CrossRef]
21. Jiang, Y.H.; Zhao, P.; Zhou, Q.; Liao, S.Y.; Jin, G.D. Petrogenesis and tectonic implications of Early Cretaceous S- and A-type granites in the northwest of the Gan-Hang rift, SE China. *Lithos* **2001**, *121*, 55–73. [CrossRef]
22. Li, Z.L.; Jing, Z.; Mao, J.W.; Santosh, M.; Yu, M.; Li, Y.; Hu, Y.; Langmuir, C.H.; Chen, Z.; Cai, X. Zircon U-Pb geochronology and geochemistry of two episodes of granitoids from the northwestern Zhejiang Province, SE China: Implication for magmatic evolution and tectonic transition. *Lithos* **2013**, *179*, 334–352. [CrossRef]
23. Li, Z.L.; Zhou, J.; Mao, J.R.; Yu, M.G.; Li, Y.Q.; Hu, Y.Z.; Wang, H.H. Age and geochemistry of the granitic porphyry from the northwestern Zhejiang Province, SE China, and its geological significance. *Acta Petrol. Sin.* **2013**, *29*, 3607–3622. (In Chinese with English Abstract)
24. Tang, Y.; Li, X.; Xie, Y.; Liu, L.; Lan, T.; Meffre, S.; Huang, C. Geochronology and geochemistry of late Jurassic adakitic intrusions and associated porphyry Mo–Cu deposit in the Tongcun area, east China: Implications for metallogenesis and tectonic setting. *Ore Geol. Rev.* **2017**, *80*, 289–308. [CrossRef]
25. Chen, Q. Simply discussion on the prospecting condition and prospecting direction of Langcun deposit. *Annu. Meet. Zhejiang Geol. Soc.* **2015**, *2015*, 99–104. (In Chinese with English Abstract)
26. Tang, Y.W.; Cui, K.; Zheng, Z.; Gao, J.; Liu, L. LA-ICP-MS U-Pb geochronology of wolframite by combining NIST series and common lead-bearing MTM as the primary reference material: Implications for metallogenesis of South China. *Gondwana Res.* **2020**, *83*, 217–231. [CrossRef]
27. Clayton, R.N.; Mayeda, T.K. The use of bromine pentafluoride in the extraction of oxygen from oxides and silicates for isotopic analysis. *Geochim. Cosmochim. Acta* **1963**, *27*, 43–52. [CrossRef]
28. Baertschi, P. Absolute 18O Content of Standard Mean Ocean Water. *Earth Planet. Sci. Lett.* **1976**, *31*, 341–344. [CrossRef]
29. Coleman, M.L.; Shepherd, T.J.; Durham, J.J.; Rouse, J.E.; Moore, G.R. Reduction of Water with Zinc for Hydrogen Isotope Analysis. *Anal. Chem.* **1982**, *54*, 993–995. [CrossRef]
30. Robinson, B.W.; Kusakabe, M. Quantitative preparation of sulfur dioxide, for sulfur-34/sulfur-32 analyses, from sulfides by combustion with cuprous oxide. *Anal. Chem.* **1975**, *47*, 45–55. [CrossRef]
31. Roedder, E. Fluid inclusions. *Rev. Mineral. Geochem.* **1984**, *12*, 644.
32. Matsuhisa, Y.; Goldsmith, J.R.; Clayton, R.N. Oxygen isotopic fractionation in the system quartz-albite-anorthite-water. *Geochim. Cosmochim. Acta* **1979**, *43*, 1131–1140. [CrossRef]
33. Taylor, H.P. The application of oxygen and hydrogen isotope studies to problems of hydrothermal alteration and ore deposition. *Econ. Geol.* **1974**, *69*, 843–883. [CrossRef]
34. Hoefs, J. *Stable Isotope Geochemistry*, 4th ed.; Springer: Berlin/Heidelberg, Germany, 2009; pp. 1–201.
35. Du, Y.D.; Yu, X.Q.; Liu, J.J.; Zhou, X.; Fu, J.Z. Characteristics of ore-forming fluids and sources of ore-forming materials in the Dongyuan W—Mo deposit, southern Anhui Province. *Geol. China* **2011**, *38*, 1334–1346. (In Chinese with English Abstract)
36. Wang, H.; Feng, C.Y.; Li, D.X.; Xiang, X.K.; Zhou, J.H. Sources of granitoids and ore-forming materials of Dahutang tungsten deposit in northern Jiangxi Province: Constraints from mineralogy and isotopic tracing. *Acta Petrol. Sin.* **2015**, *31*, 725–739. (In Chinese with English Abstract)
37. Ohmoto, H. Systematics of sulfur and carbon isotopes in hydrothermal ore deposits. *Econ. Geol.* **1972**, *67*, 551–578. [CrossRef]
38. Shinohara, H. Exsolution of immiscible vapor and liquid phases from a crystallizing silicate melt: Implications for chlorine and metal transport. *Geochim. Cosmochim. Acta* **1994**, *58*, 5215–5221. [CrossRef]

39. Kamenetsky, V.S.; Wolfe, R.C.; Eggins, S.M.; Mernagh, T.P.; Bastrakov, E. Volatile exsolution at the Dinkidi Cu-Au porphyry deposit, Philippines: A melt-inclusion record of the initial ore-forming process. *Geology* **1999**, *27*, 691–694. [CrossRef]
40. Wood, S.A.; Samson, I.M. The hydrothermal geochemistry of tungsten in granitoid environments: I. relative solubilities of ferberite and scheelite as a function of T, P, pH, and mNaCl. *Econ. Geol.* **2000**, *95*, 143–182. [CrossRef]
41. Ni, P.; Wang, X.D.; Wang, G.G.; Huang, J.B.; Pan, J.Y.; Wang, T.G. An infrared microthermometric study of fluid inclusions in coexisting quartz and wolframite from Late Mesozoic tungsten deposits in the Gannan metallogenic belt, South China. *Ore Geol. Rev.* **2015**, *65*, 1062–1077. [CrossRef]
42. Lecumberri-Sanchez, P.; Vieira, R.; Heinrich, C.A.; Pinto, F.; Wälle, M. Fluid-rock interaction is decisive for the formation of tungsten deposits. *Geology* **2017**, *45*, 579–582. [CrossRef]
43. Yang, J.H.; Zhang, Z.; Peng, J.T.; Liu, L.; Leng, C.B. Metal source and wolframite precipitation process at the Xihuashan tungsten deposit, South China: Insights from mineralogy, fluid inclusion and stable isotope. *Ore Geol. Rev.* **2019**, *111*, 102965. [CrossRef]
44. Korges, M.; Weis, P.; Volker, L.; Laurent, O. Depressurization and boiling of a single magmatic fluid as a mechanism for tin-tungsten deposit formation. *Geology* **2018**, *46*, 75–78. [CrossRef]
45. Wei, W.F.; Hu, R.Z.; Bi, X.W.; Peng, J.T.; Shi, S.H. Infrared microthermometric and stable isotopic study of fluid inclusions in wolframite at the Xihuashan tungsten deposit, Jiangxi province, China. *Miner. Depos.* **2012**, *47*, 589–605. [CrossRef]
46. Pan, J.Y.; Ni, P.; Wang, R.C. Comparison of fluid processes in coexisting wolframite and quartz from a giant vein-type tungsten deposit, South China: Insights from detailed petrography and LA-ICP-MS analysis of fluid inclusions. *Am. Mineral.* **2019**, *104*, 1092–1116. [CrossRef]
47. Wang, H.; Feng, C.Y.; Li, R.X.; Li, C.; Zhao, C.; Chen, X.; Wang, G.H. Ore-forming mechanism and fluid evolution processes of the Xingluokeng tungsten deposit, western Fujian Province: Constraints form in-situ trace elemental and Sr isotopic analyses of scheelite. *Acta Petrol. Sin.* **2021**, *37*, 698–716. (In Chinese with English Abstract) [CrossRef]
48. Liu, J.; Li, W.C.; Zhu, X.P.; Li, C.; Zhou, Q.; Yang, F.C. Origin and evolution of ore-forming fluids of the Larong W-(Mo) deposit, eastern Tibet: Constraints from fluid inclusions, H–O isotopes, and scheelite geochemistry. *Ore Geol. Rev.* **2020**, *124*, 103620. [CrossRef]
49. Yang, Y.F.; Li, N.; Chen, Y.J. Fluid inclusion study of the Nannihu giant porphyry Mo-W deposit, Henan Province, China: Implications for the nature of porphyry ore-fluid systems formed in a continental collision setting. *Ore Geol. Rev.* **2012**, *46*, 83–94. [CrossRef]
50. Higgins, N.C. Fluid inclusion evidence for the transport of tungsten by carbonate complexes in hydrothermal solutions. *Can. J. Earth Sci.* **1980**, *17*, 823–830. [CrossRef]
51. Liu, X.C.; Zhang, D.H. The efficient mechanisms for precipitating wolframite: CO_2 escaping. *Int. J. Geomech.* **2019**, *25*, 19–26. [CrossRef]